UC Berkeley

UC Berkeley Previously Published Works

Title

Mapping charge excitations in generalized Wigner crystals

Permalink

https://escholarship.org/uc/item/3fg2c302

Journal

Nature Nanotechnology, 19(5)

ISSN

1748-3387

Authors

Li, Hongyuan
Xiang, Ziyu
Regan, Emma
et al.

Publication Date

2024-05-01

DOI

10.1038/s41565-023-01594-x

Copyright Information

This work is made available under the terms of a Creative Commons Attribution License, available at https://creativecommons.org/licenses/by/4.0/

Peer reviewed

eScholarship.org Powered by the California Digital Library
University of California

Mapping Charge Excitations in Generalized Wigner Crystals

Hongyuan Li[1, 2, 3, 8], *Ziyu Xiang*[1, 2, 3, 8], *Emma Regan*[1, 2, 3], *Wenyu Zhao*[1], *Renee Sailus*[4], *Rounak Banerjee*[4], *Takashi Taniguchi*[5], *Kenji Watanabe*[6], *Sefaattin Tongay*[4], *Alex Zettl*[1, 3, 7], *Michael F. Crommie*[1, 3, 7]* and *Feng Wang*[1, 3, 7]*

[1]Department of Physics, University of California at Berkeley, Berkeley, CA, USA.

[2]Graduate Group in Applied Science and Technology, University of California at Berkeley, Berkeley, CA, USA.

[3]Materials Sciences Division, Lawrence Berkeley National Laboratory, Berkeley, CA, USA.

[4]School for Engineering of Matter, Transport and Energy, Arizona State University, Tempe, AZ, USA.

[5]International Center for Materials Nanoarchitectonics, National Institute for Materials Science, Tsukuba, Japan

[6]Research Center for Functional Materials, National Institute for Materials Science, Tsukuba, Japan

[7]Kavli Energy Nano Sciences Institute at the University of California Berkeley and the Lawrence Berkeley National Laboratory, Berkeley, CA, USA.

[8]These authors contributed equally: Hongyuan Li and Ziyu Xiang

Abstract: Transition metal dichalcogenide (TMD)-based moiré superlattices exhibit strong electron-electron correlations, thus giving rise to strongly correlated quantum phenomena such as generalized Wigner crystal states, a delicate electron crystalline phase[1-11]. The evidence of Wigner crystal in TMD moire superlattice has been widely reported in various optical spectroscopy[1,2] and electrical conductivity measurements[3,11], while their microscopic nature remains mostly unknown. Previous work on imaging of 2D Wigner crystal only provided limited information such as lattice structure[5]. Important physical properties of the Wigner crystal such as its elementary excitations and the corresponding energy gaps are still unclear microscopically. Theoretical studies predict that unusual quasiparticle excitations across the correlated gap between upper and lower Hubbard bands can arise due to long-range Coulomb interactions in generalized Wigner crystal states[7,9,12]. The microscopic probe of such quasiparticle excitations, however, is non-trivial because of the fragility and low excitation energy of the Wigner crystal. Here we describe a new scanning single-electron charging (SSEC) spectroscopy technique with nanometer spatial resolution and single-electron charge resolution that enables us to directly image electron and hole wavefunctions and to determine the thermodynamic gap of generalized Wigner crystal states in twisted WS_2 moiré heterostructures. High-resolution SSEC spectroscopy was achieved by combining scanning tunneling microscopy (STM) with a monolayer graphene sensing layer, thus enabling the generation of individual electron and hole quasiparticles in generalized Wigner crystals. We show that electron and hole quasiparticles have complementary wavefunction distributions and that thermodynamic gaps of order 50meV exist for the 1/3 and 2/3 generalized Wigner crystal states.

A Wigner crystal is the crystalline phase of electrons stabilized at low electron density when long-range Coulomb interactions dominate over quantum fluctuations in electron motion[13]. The recent discovery of flat moiré minibands in van der Waals heterostructures has opened a new route to realize Wigner crystal states at zero magnetic field[1-8]. A variety of generalized Wigner crystal states have been reported in transition metal dichalcogenide (TMDC) moiré superlattices[1-5], and real-space imaging of the electron lattice of generalized Wigner crystals has been performed using a new form of non-invasive STM imaging[5]. A microscopic understanding of elementary excitations in generalized Wigner crystal, however, is still lacking. Theoretical studies predict that unusual quasiparticle excitations across the correlated gap between upper and lower Hubbard bands can arise due to long-range Coulomb interactions in generalized Wigner crystal states[7,9,12]. However, because of the fragile electron lattice and small energy scale, it is challenging to image quasiparticle (e.g., electron/hole) wavefunctions and to spectroscopically determine the correlated gaps of generalized Wigner crystals.

Several scanning probe microscopy techniques have previously been developed to probe fragile correlated states, such as scanning charge accumulation microscopy[14-16] and scanning single-electron transistor microscopy[17-19]. The spatial resolution of these microscopy tools, however, is typically limited to ~100nm, and so is not sufficient to image generalized Wigner crystal quasiparticle states at the single unit cell level. Here we describe a new scanning single-electron charging (SSEC) spectroscopy that has ~1 nm spatial resolution as well as single electron sensitivity. SSEC spectroscopy technique combines STM with a monolayer graphene sensing layer and enables local manipulation of individual electron- and hole-quasiparticles in generalized Wigner crystals via STM tip-based local gating. It enables direct visualization of quasiparticle excitations and spectroscopic determination of the thermodynamic gap of

generalized Wigner crystals. Using this technique, we observe that electron and hole quasiparticles excitations exhibit complementary wavefunction distributions and that thermodynamic gaps of order 50meV exist for the 1/3 and 2/3 generalized Wigner crystal states.

Fig. 1a shows the design of the sample and the measurement scheme. The sample is a near-60° twisted WS_2 (t-WS_2) moiré heterostructure encapsulated in hBN layers. It is dual gated by a monolayer of graphene on top (the top gate) and graphite on the bottom (the bottom gate). The hBN dielectric layer thicknesses for the top and bottom gates are 5.8nm and 37nm, respectively. Sample fabrication details are included in Methods. The charge carrier densities of the t-WS_2 and the top graphene sensing layer are tuned independently by applying a bottom gate voltage V_{BG} and a top gate voltage V_{TG}. A bias voltage (V_{bias}) is applied between the graphene top gate (otherwise known as the sensing layer) and the STM tip. Application of V_{bias} allows electrons in the t-WS_2 moiré heterostructure to be manipulated by local tip-gating and to be detected through charging events measured via the tunnel current to the graphene sensing layer.

Conventional STM measurement of the graphene sensing layer provides information on the corrugation of the heterostructure sample as shown in Fig.1b. The thin top graphene and hBN bend conformally and thus inherit the topography of the t-WS_2 moiré superlattice. Two sets of moiré superlattices with distinct periods are observed. The larger periodicity (9 nm) originates from the t-WS_2 moiré superlattice which has a twist angle of 58°, while the smaller periodicity (~1.5 nm) corresponds to the moiré superlattice formed by the top graphene and hBN which has a twist angle of 9.6°. The 58° t-WS_2 moiré superlattice exhibits a triangular lattice with three types of high symmetry stacking regions in each unit cell: a bright region ($B^{S/S}$ stacking), a dark region (AB stacking), and a medium height region ($B^{W/W}$ stacking)[20] (see Fig. 1b inset). The

bonding arrangements of the $B^{S/S}$, AB, and $B^{W/W}$ stacking orders are sketched on the left side of Fig. 1b.

Figure 1c-f illustrates the dual role of the STM tip in SSEC spectroscopy. In Fig. 1c the biased STM tip is seen to act as a local gate on the t-WS_2 because its electrical field partially penetrates the monolayer graphene. This is because graphene has a small electron density of states and weak screening, especially when its Fermi level is near the Dirac point. When the sample-tip bias $V_{bias} = V_{bias0}$, where V_{bias0} is a small offset bias voltage that cancels the work function difference between the tip and the graphene the tip exerts no local gating effect (Fig. 1d). With a decreased (increased) V_{bias}, positive (negative) charge accumulates at the tip apex and generates local band bending in the t-WS_2 due to E-field penetrating through the monolayer graphene (Figs. 1e and 1f). With sufficiently strong band bending a single electron (hole) quasiparticle will be injected into the t-WS_2. The added charge due to this tip-induced quasiparticle excitation will, in turn, alter the tip-graphene tunnel current via long-range Coulomb interactions (see more discussion in the SI). SSEC spectroscopy has some similarity to capacitance spectroscopy in that the tip bias voltage drives charging of the t-WS_2. However, unlike conventional capacitance spectroscopy, SSEC spectroscopy locally manipulates individual electrons/holes in the heterostructure and is responsive to individual charge excitation through the tunnel current to the graphene sensing layer. A spatial resolution of ~ 1 nanometer can be achieved in SSEC spectroscopy for thin top hBN layers having a thickness of several nanometers. It also shares similarities with the tip-induced charging behavior in molecules and quantum dots observed in previous scanning probe measurements[21-26]. However, the SSEC spectroscopy enables a quantitative thermodynamic measurement of correlated electrons, that is beyond the capability of previous single-electron charging studies. The key difference lies in the

application of the graphene sensing layer, which not only decouples the single-charge excitation and tunneling current measurement but also minimizes the tip perturbation while remaining a high spatial resolution.

Figure 2a shows the backgate voltage (V_{BG}) dependence of the dI/dV spectra of the tip-graphene tunnel junction when the tip is placed over the $B^{S/S}$ site of the moiré unit cell (see SI for stacking site dependence of the dI/dV spectra). We started by setting the top gate voltage to V_{TG} = 0.52V, which shifts the t-WS_2 chemical potential up to the conduction band edge while keeping the graphene Fermi level close to the Dirac point[5]. Under these conditions increasing the backgate voltage, V_{BG}, increases the global electron doping in the t-WS_2 layers. The resulting dI/dV measurement of the sensing layer is dominated by a broad increase in the dI/dV signal for increased V_{bias} regardless of polarity, which mostly reflects the local density of states of graphene and does not show an obvious dependence on V_{BG} (i.e. on the t-WS_2 doping). The impact of electrical charge added to the t-WS_2 moiré superlattice is better seen by normalizing the dI/dV spectra at each V_{BG} by the averaged dI/dV spectrum over all V_{BG} values as seen in Fig. 2b (see the SI for normalization details). This normalization removes the broad rising background and reveals multiple dispersive bright lines that correspond to peaks in dI/dV that shift in energy with applied V_{BG}. These peaks are clustered around several electron doping levels in the t-WS_2 moiré superlattice (i.e., different V_{BG} values), as denoted by horizontal arrows in Fig. 2b. Their V_{BG} values correspond to t-WS_2 electron filling factors of n = 0, 1/3, 2/3, 1 (as labeled in red), where n is the number of electrons per moiré site. The filling factors shown here are based on carrier densities extracted using the device capacitance as described in reference[5]. Our SSEC imaging (see SI and Fig.3) is also consistent with these filling factors.

The dI/dV spectra of Fig. 2b show two or more dispersive lines clustered around each correlated insulating state at n = 1/3, 2/3, and 1. To better understand this behavior Fig. 2c shows higher resolution V_{BG}-dependent dI/dV spectra near the n = 2/3 generalized Wigner crystal state (the phase space inside the white dashed box in Fig. 2b). Two bright dispersive lines with similar slope move together through the V_{BG} region associated with the n = 2/3 state, as well as several weaker features nearby. We note that the V_{BG}-independent vertical peaks and dips around V_{bias} = 0 in Fig. 2b,c are artifacts due to the numerical normalization. Figure 2d displays a horizontal line cut of Fig. 2c at V_{BG} = 1.60V, where clear dI/dV peaks (labeled with vertical arrows) can be observed at the V_{bias} positions of the bright lines in Fig. 2c. These dI/dV peaks do not mark the energy locations of resonances in the local density of states (LDOS), but rather arise from electron and hole charging events in the generalized Wigner crystal states of t-WS_2.

To understand this, we look to the sketch in Fig. 2e that illustrates the charging diagram of the t-WS_2 moiré superlattice in the n = 2/3 state. There are three different regimes as shown in Fig. 2f: the "intrinsic" generalized Wigner crystal insulator phase (I) (solid red dots mark the locations of electrons in the moiré unit cell while open circles mark empty cells), the electron excitation regime (E) where an electron (blue solid dot in Fig. 2f) is injected below the tip at a large negative V_{bias}, and the hole excitation regime (H) where a hole (blue open circle in Fig. 2f) is injected at a large positive V_{bias}. These regimes are separated by two dispersive lines in the V_{BG}-V_{bias} parameter space in Fig. 2e with the slope of the dispersive lines being determined by the efficiency of the tip as an effective top gate relative to chemical potential shifts induced by the bottom gate. Starting from the intrinsic regime (e.g., Fig. 1d), a reduction of V_{bias} causes the tip to become positively charged. Crossing the boundary from (I) to (E) corresponds to pushing the UHB energetically below the t-WS_2 chemical potential μ_{tWS_2} and locally inducing an

electron charging event (Fig. 1e). Similarly, if V_{bias} is increased and crosses the boundary from (I) to (H) then the LHB is energetically pushed above μ_{tWS_2}, resulting in a local hole charging event (Fig. 1f). These charge excitations alter the tunnel junction conductance and result in a peak in the dI/dV spectra (see more discussion in the SI). The dispersive dI/dV peaks in Figs. 2b,c correspond to the electron/hole excitation boundaries sketched in Fig. 2e. The reason that the intrinsic region does not bracket $V_{bias} = 0$ is most likely because of the work function difference between the tip and the graphene sensing layer. Additional weaker dI/dV peak features observed in Fig. 2c at higher positive (negative) V_{bias} correspond to the injection of additional electrons and holes at nearby moiré cells adjacent to the tip location.

To establish our assignment of the features seen in Fig.2 as electron and hole excitations of the generalized Wigner crystal, we directly image these charging events using SSEC spectroscopy. Fig. 3a displays an STM topography image of a highly defect-free t-WS_2 moiré region chosen for imaging electron/hole excitations. Fig. 3b shows a dI/dV map measured over this same area at $V_{BG} = 1.50V$, $V_{TG} = 0.52V$, and $V_{bias} = -0.59V$, which corresponds to the electron excitation boundary denoted by the filled circle in Fig. 2c. A triangular lattice of bright dots is seen with a period larger than the underlying moiré superlattice by a factor of $\sqrt{3}$. This new triangular lattice reflects the wavefunction distribution of the excited electron in the generalized n = 2/3 Wigner crystal. To confirm that this pattern originates from tip-induced electron excitations we tested how it evolves with V_{bias}. A typical aspect of charging features is "ring expansion" with increased bias[21-26] because the tip can then induce charging events from more distant positions. Figs. 3d-g show the evolution of the charging rings with increasing $|V_{bias}|$, obtained at $V_{BG} = 1.50V$ and $V_{TG} = 0.52V$. The electron charging signal at the different moiré

unit cells is seen to expand into a wide charging ring with increasingly negative V_{bias}, precisely as expected for electron injection.

Fig. 3c shows a dI/dV map taken at the hole excitation boundary for n = 2/3 filling, corresponding to the open circle in Fig. 2c (V_{BG} = 1.65V, V_{TG} = 0.52V, and V_{bias} = -0.14V). A honeycomb lattice of bright dots (open circles) here reflects the wavefunction of hole excitations in this generalized Wigner crystal. The tip bias dependence of this pattern also confirms its origin as shown in Figs. 3h-k. Here the hole charging signal in the different moiré unit cells is seen to expand into a wider charging ring for increasingly positive V_{bias}. Note in Fig. 3h-k V_{TG} is set at 0.49V instead of the original 0.52V so that a nonzero hole charging signal can be observed over a wider V_{bias} range (extending to the positive V_{bias} side) and hence we can measure the continuous evolution of the charging rings as a function of V_{bias} (see V_{TG} dependence of the dI/dV spectra in SI).

The complementarity of the electron and hole excitation wavefunctions of the generalized Wigner crystal state can be seen by overlaying the hollow circles and solids dots of Figs. 3b,c onto the topography of Fig. 3a. Both the hollow *and* solid circles are seen to be localized in the $B^{W/W}$ stacking regions, where the lowest-energy conduction moiré flat bands are predicted to reside[20]. The electron excitation distribution (red dots) and the hole excitation distribution (open circles) combine perfectly to yield the full moiré superlattice. Hole excitations correspond precisely to the filled electron locations for an n = 2/3 generalized Wigner crystal (i.e., a honeycomb lattice) whereas electron excitations occur at the hollow centers of the honeycomb lattice. This is the pattern that one might intuitively expect from classical electrostatic reasoning.

Since the thermodynamic gap of a correlated state is the chemical potential difference for adding a single hole or electron, it is possible to extract the thermodynamic gap of generalized

Wigner crystals from our SSEC spectra. To see this we define the energy difference between the chemical potential and LHB as Δ_h (Fig. 1d), and the bias applied to the tip to create a hole excitation as V_h. We then write $\Delta_h = \alpha_h e V_h$, where α_h is a geometric constant defined by the tip-gating efficiency when the tip is above a hole site (e is the charge of an electron). Similarly, we can write $\Delta_e = \alpha_e(-e)V_e$ where Δ_e is the energy difference between the chemical potential and UHB, and the factors V_e and α_e are defined for electron excitations. If $\alpha_e = \alpha_h = \alpha$, then the thermodynamic gap, $\Delta = \Delta_e + \Delta_h$, can be written as

$$\Delta = \alpha e(V_h - V_e) = \alpha e \Delta V_{bias}, \quad (1)$$

where ΔV_{bias} is the experimental sample-tip bias difference measured between the hole excitation and electron excitation boundaries as shown in Figs. 2c-e (see more details on the determination of ΔV_{bias} in SI). A key requirement in this analysis is that the capacitive coupling between the tip and surface is equivalent for electron and hole excitations (i.e., $\alpha_e = \alpha_h$). This requirement is satisfied in the measurements shown in Fig. 2 which were performed with the tip positioned above the $B^{S/S}$ site in the t-WS_2 moiré unit cell, which is the same distance to the nearest excited electron or hole.

In order to obtain a quantitative value of the generalized Wigner crystal thermodynamic gap, Δ, we must determine the value of α. It is also useful to introduce the backgate coupling parameter β such that the electric potential change at the t-WS_2 moiré site is $\Delta\Phi = e\alpha V_{bias} - e\beta V_{BG}$. The ratio, α/β, is an experimentally accessible quantity since it is the slope of the dispersive features observed in Figs. 2b,c (charging occurs when the Φ-dependent UHB or LHB, becomes equal to the chemical potential). The value of α is obtained by the experimentally determined ratio α/β through a one-to-one correspondence between α and α/β. This correspondence relation between α and α/β is obtained through numerical simulation of the tip-

surface electrostatics (see SI for simulation details). In the simulation we model the backgate as a metallic plate. Due to the unknown geometry of the STM tip, we model the tip in two extreme situations: (1) as a metallic cone and (2) as a metallic sphere. The screening by Dirac electrons in the graphene sensing layer is included in the simulation (see SI for details). The t-WS_2 layer is regarded as a thin insulator since it is in a correlated insulating phase. To obtain α, we monitor the local electric potential change, $\Delta\Phi$, in the t-WS_2 layer that is induced by applying nonzero V_{bias}. The main variable parameters in the simulation are the tip geometry (cone angle θ for the conic tip model and sphere radius for the spherical tip model) and the tip height (h). Although these parameters are hard to obtain experimentally, our simulation results indicate that the correspondence relation between α and α/β is almost independent of the tip shape and height (see Fig. S6 in the SI) where the uncertainty in the correspondence relation due to the unknown tip geometry is less than 3%. With such a tip-geometry-independent correspondence relation, we are thus able to determine $\alpha = 0.160 \pm 0.005$ from the experimentally measured ratio $\frac{\alpha}{\beta} = 0.51 \pm 0.01$. From Eq. (1) this results in the following experimental thermodynamic gaps for the n = 1/3, 2/3, and 1 correlated states: $\Delta_{n=1/3} = 50 \pm 11\text{meV}$, $\Delta_{n=2/3} = 45 \pm 11\text{meV}$, and $\Delta_{n=1} = 106 \pm 29\text{meV}$ (the uncertainty here is calculated from both the standard deviation in our measurement of ΔV_{bias} and the uncertainty of α).

In conclusion, we have demonstrated a non-invasive high-resolution microscopic tool that enables us to induce electron/hole excitations locally in 2D generalized Wigner crystal systems. This technique allows us to measure the thermodynamic gaps of generalized Wigner crystals having different filling factors and to map their electron and hole excitations. This technique should be applicable to the characterization of other fragile correlated electron systems.

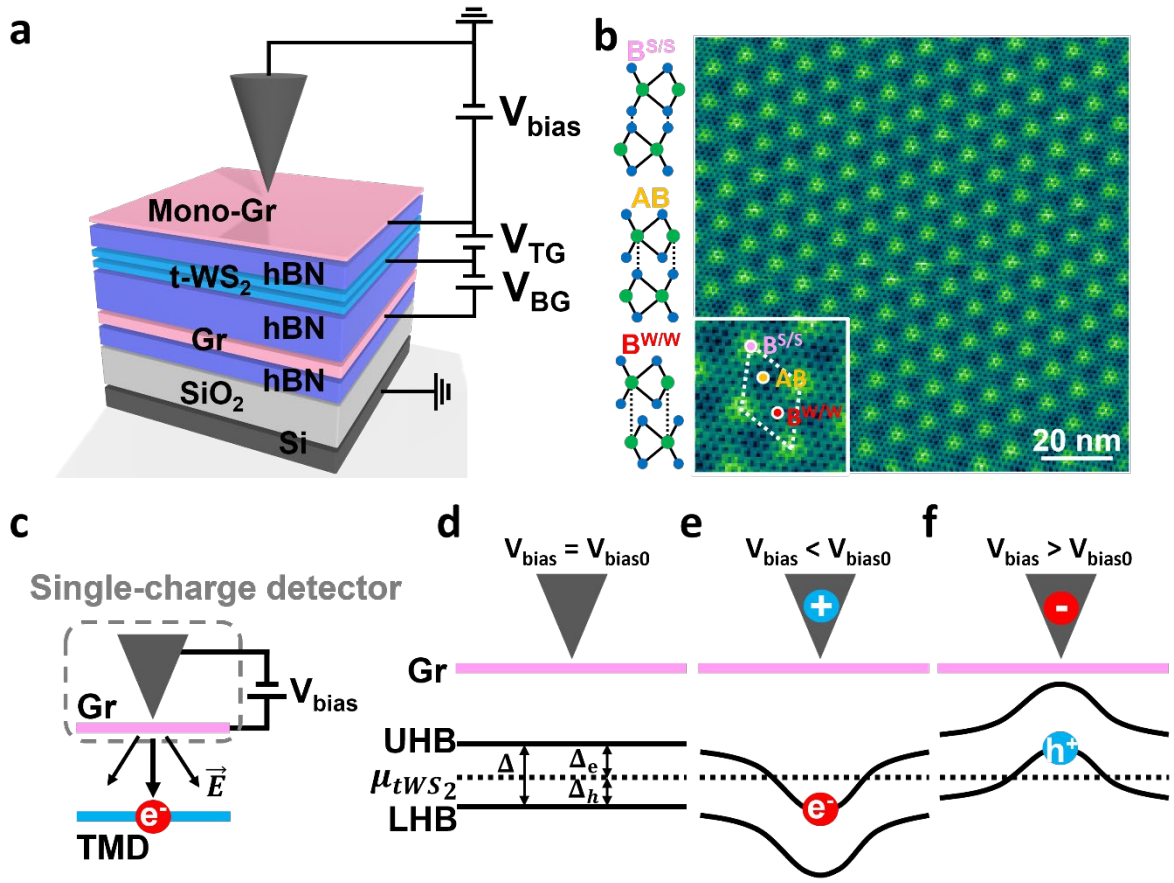

Figure 1. Scanning single-electron charge spectroscopy measurement of a twisted bilayer WS_2 moiré superlattice. a. Schematic of the dual-gated near-60° twisted bilayer WS_2 (t-WS_2) moiré superlattice device. The top hBN thickness (5nm) is slightly smaller than the moiré lattice constant (9nm). Top gate (V_{TG}) and bottom gate (V_{BG}) voltages are separately applied to independently control the carrier densities in the t-WS_2 superlattice and top graphene sensing layer. **b**. A typical large-scale topography image of the top graphene (V_{bias} = -0.62V and I = 150 pA). Three different stacking regions are labeled in the close-up image in the inset: $B^{S/S}$ stacking (pink dots), AB stacking (yellow dots), and $B^{W/W}$ (red dots). The structures of the $B^{S/S}$, AB, and $B^{W/W}$ stacking are illustrated in the left pannel **c**. Illustration of scanning single-electron charge (SSEC) spectroscopy. The electric field from the tip bias partially penetrates the graphene and induces quasiparticle excitations in the t-WS_2. The tip-graphene tunnel junction detects changes in the number of electrons in the t-WS_2 due to long range Coulomb interactions. **d-f**. Illustration of tip-induced quasiparticle excitation in a correlated insulator. Solid curves represent the lower

Hubbard band (LHB) and upper Hubbard band (UHB), while dashed line represents the chemical potential μ_{tWS_2}. (**d**) For $V_{bias} = V_{bias0}$, where V_{bias0} is the offset bias voltage that cancels the work function difference between the tip and the top sensing layer graphene, the LHB and UHB are uniform. (**e**) For large $V_{bias} < V_{bias0}$ the UHB is pushed beneath E_F by tip-gating, inducing a local electron excitation. (**f**) For large $V_{bias} > V_{bias0}$ tip-gating induces a local hole excitation. The gap between the UHB and LHB is labeled as Δ while the gap between μ_{tWS_2} and UHB (LHB) is labeled as Δ_e (Δ_h).

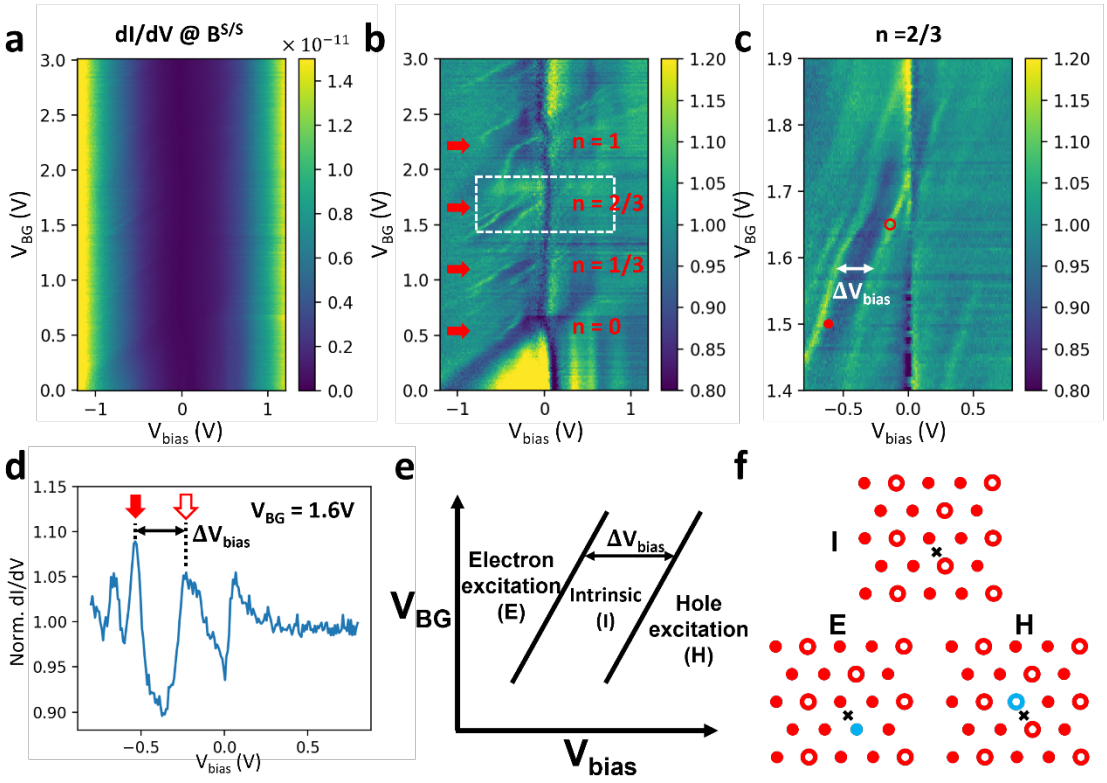

Figure 2. STS study of quasiparticle excitations in generalized Wigner crystals. a. dI/dV spectra of the graphene sensing layer as a function of sample-tip bias (V_{bias}) and backgate voltage (V_{BG}) (measured with tip held over the t-WS_2 $B^{S/S}$ site). V_{TG} is fixed at 0.52V. **b**. Normalized form of the dI/dV spectra shown in **a**. The dI/dV spectrum at each V_{BG} is normalized by the average dI/dV spectrum for all V_{BG} values (see SI for details). Dispersive bright lines corresponding to dI/dV peaks are clustered around the filling factors n = 0, 1/3, 2/3, 1 (labeled in red). **c**. High-resolution dI/dV spectra corresponding to the n = 2/3 state measured over the range enclosed by the white box in **b**. Two bright dispersive lines with similar slopes exist on opposite sides of the n=2/3 state and correspond to electron charging events (solid dot) and hole charging events (open circle), The ΔV_{bias} offset between them is marked in white. **d**. dI/dV line-cut of **c** at V_{BG} = 1.60V shows peaks corresponding to dispersive features in **c** labeled with a solid arrow (electron charging) and an open arrow (hole charging) that are offset from each other by ΔV_{bias}.

e. Schematic shows the charging regimes of the t-WS_2 moiré superlattice near the n = 2/3 state. (I) marks the intrinsic generalized Wigner crystal insulator phase, (E) marks the electron excitation regime, and (H) marks the hole excitation regime. The charging regimes are separated by two dispersive lines in the V_{BG}-V_{bias} parameter space that are offset from each other by ΔV_{bias}. **f**. Real space sketch of the intrinsic (I), electron excitation (E), and hole excitation (H) regimes. Electron-filled sites (solid dots) and empty sites (open circles) of the n = 2/3 generalized Wigner crystal as shown. Tip-induced electron excitation is marked by a solid blue dot and hole excitation by a blue open circle. The back cross labels the tip position.

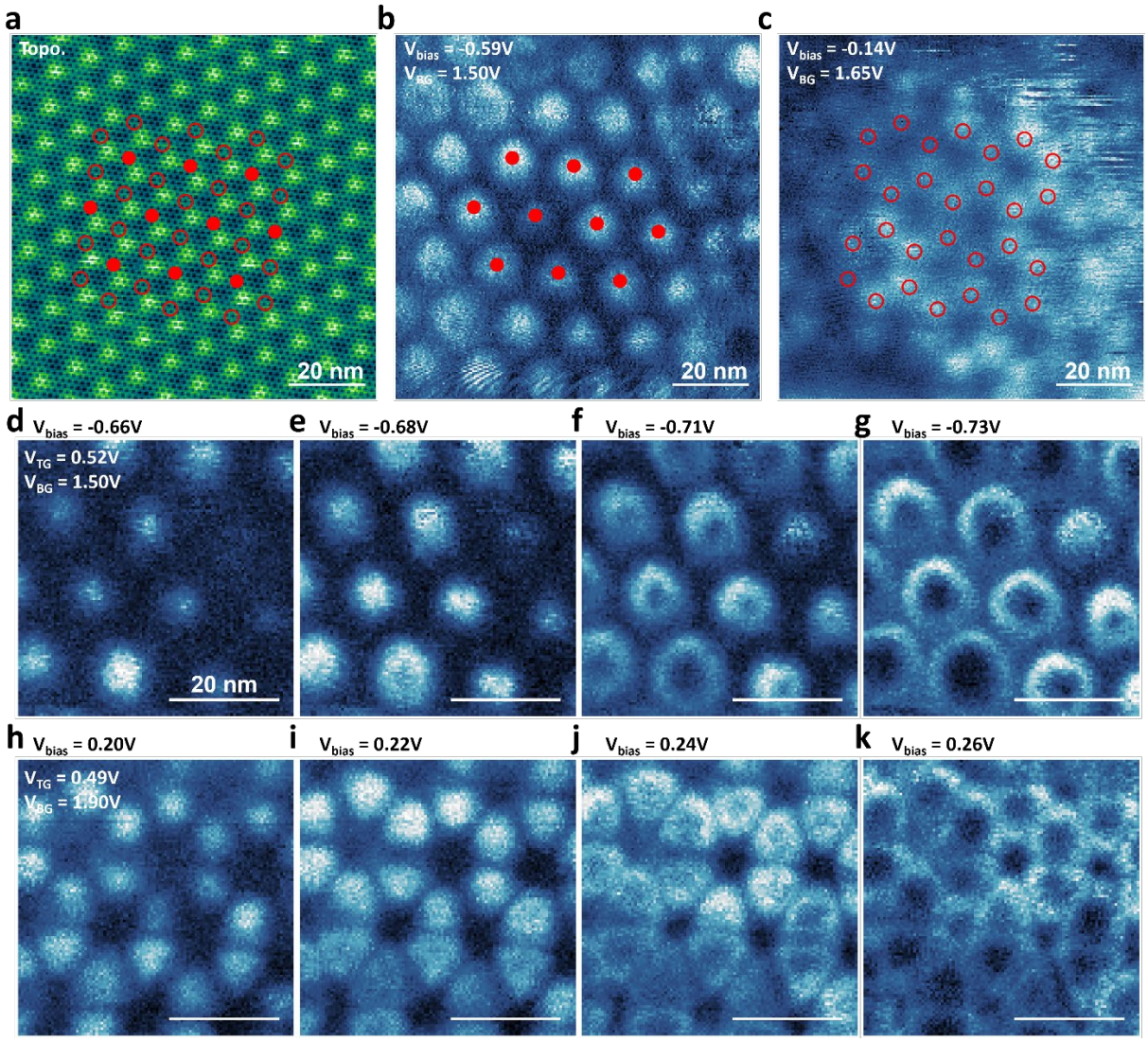

Figure 3. Mapping electron and hole excitations of the n = 2/3 generalized Wigner crystal. **a**. STM topography image of graphene sensing layer shows the t-WS2 moiré superlattice (V_{bias} = -0.59V, I = 150pA). **b**. dI/dV map of same area as (**a**) for applied voltages corresponding to the electron excitation boundary (V_{BG} = 1.50V, V_{TG} = 0.52V, V_{bias} = -0.59V). Sites of electron excitations are marked with solid red dots. **c**. dI/dV map of same area as (**a**) for voltages corresponding to the hole excitation boundary (V_{BG} = 1.65V, V_{TG} = 0.52V, V_{bias} = -0.14V). Sites of hole excitations are marked with open circles. **d-g**. Evolution of dI/dV maps of the electron charging peak of the n = 2/3 state with increasingly negative V_{bias}. The electron charging signals widen into a growing circle at each moiré site as V_{bias} becomes more negative. **h-k**. Evolution of dI/dV maps of the hole charging peak of the n = 2/3 state with increasingly positive V_{bias}. The hole charging signal widens into a growing circle as V_{bias} becomes more positive. The solid dots in **b** and open circles in **c** are overlaid in **a** and are seen to be perfectly complementary. (**d-k**) share the same scale bar.

Corresponding Author

* Email: crommie@physics.berkeley.edu (M.C.) and fengwang76@berkeley.edu (F.W.).

Author Contributions

H. L., M.C., and F.W. conceived the project. H.L. and Z.X. performed the STM measurement, H.L., Z.X., E. R., and W.Z. fabricated the heterostructure device. R.S., R.B. and S.T. grew the WS_2 crystals. K.W. and T.T. grew the hBN single crystal. All authors discussed the results and wrote the manuscript.

Notes

The authors declare no financial competing interests.

ACKNOWLEDGMENT

This work was primarily funded by the U.S. Department of Energy, Office of Science, Office of Basic Energy Sciences, Materials Sciences and Engineering Division under Contract No. DE-AC02-05-CH11231 (van der Waals heterostructure program KCFW16) (device electrode

preparation and STM spectroscopy). Support was also provided by the US Army Research Office under MURI award W911NF-17-1-0312 (device layer transfer), and by the National Science Foundation Award DMR-1807233 (surface preparation). S.T acknowledges support from DOE-SC0020653 (materials synthesis), NSF DMR-1955889 (magnetic measurements), NSF CMMI-1933214, NSF 2206987, NSF ECCS 2052527, DMR 2111812, and CMMI 2129412. K.W. and T.T. acknowledge support from the Elemental Strategy Initiative conducted by the MEXT, Japan, Grant Number JPMXP0112101001, JSPS KAKENHI Grant Number JP20H00354 and the CREST(JPMJCR15F3), JST for bulk hBN crystal growth and analysis.

Methods

Sample fabrication: The encapsulated near-60° twisted WS_2 (t-WS_2) moire heterostructure stack was fabricated using a micro-mechanical stacking technique[27]. A poly(propylene) carbonate (PPC) film stamp was used to pick up all exfoliated 2D material flakes. The 2D material layers in the main heterostructure region were picked up in the following order: substrate hBN, graphite, bottom hBN, first WS_2 monolayer, second monolayer, graphene nanoribbon array (not shown in Fig. 1), top hBN, and then monolayer graphene. The graphene nanoribbon array serves as a contact electrode for the t-WS_2 and is fabricated by an electrode-free local anodic oxidization (EFLAO) lithography technique[28]. The two WS_2 monolayers are obtained by cutting an originally complete single flake into two pieces using EFLAO to precisely control their crystal directions. The PPC film together with the stacked sample was then peeled, flipped over, and transferred onto a Si/SiO_2 substrate (SiO_2 thickness 285nm). The PPC layer was subsequently removed using ultrahigh

vacuum annealing at 230 °C, resulting in an atomically clean heterostructure suitable for STM measurements. A 50nm Au and 5nm Cr metal layer was evaporated through a shadow mask to form electrical contacts to the graphene layers.

STS measurement: A modulation of 25mV amplitude and 500~900 Hz frequency was applied to the tip bias to obtain the dI/dV signal.

Supplementary Materials

Data availability

The data supporting the findings of this study are included in the main text and in the Supplementary Information files, and are also available from the corresponding authors upon request.

Reference

1 Regan, E. C. *et al.* Mott and generalized Wigner crystal states in WSe 2/WS 2 moiré superlattices. *Nature* **579**, 359-363 (2020).

2 Xu, Y. *et al.* Correlated insulating states at fractional fillings of moiré superlattices. *Nature* **587**, 214-218 (2020).

3 Huang, X. *et al.* Correlated insulating states at fractional fillings of the WS2/WSe2 moiré lattice. *Nature Physics* **17**, 715-719 (2021).

4 Jin, C. *et al.* Stripe phases in WSe 2/WS 2 moiré superlattices. *Nature Materials*, 1-5 (2021).

5 Li, H. *et al.* Imaging two-dimensional generalized Wigner crystals. *Nature* **597**, 650-654 (2021).

6 Wang, L. *et al.* Correlated electronic phases in twisted bilayer transition metal dichalcogenides. *Nature materials*, 1-6 (2020).

7 Pan, H., Wu, F. & Sarma, S. D. Quantum phase diagram of a Moiré-Hubbard model. *Physical Review B* **102**, 201104 (2020).

8 Tang, Y. *et al.* Simulation of Hubbard model physics in WSe 2/WS 2 moiré superlattices. *Nature* **579**, 353-358 (2020).

9 Padhi, B., Chitra, R. & Phillips, P. W. Generalized Wigner crystallization in moiré materials. *Physical Review B* **103**, 125146 (2021).
10 Padhi, B., Setty, C. & Phillips, P. W. Doped twisted bilayer graphene near magic angles: proximity to Wigner crystallization, not Mott insulation. *Nano letters* **18**, 6175-6180 (2018).
11 Li, T. *et al.* Charge-order-enhanced capacitance in semiconductor moir\'e superlattices. *arXiv preprint arXiv:2102.10823* (2021).
12 Slagle, K. & Fu, L. Charge transfer excitations, pair density waves, and superconductivity in moiré materials. *Physical Review B* **102**, 235423 (2020).
13 Wigner, E. On the interaction of electrons in metals. *Physical Review* **46**, 1002 (1934).
14 Tessmer, S., Glicofridis, P., Ashoori, R., Levitov, L. & Melloch, M. Subsurface charge accumulation imaging of a quantum Hall liquid. *Nature* **392**, 51-54 (1998).
15 Finkelstein, G., Glicofridis, P., Ashoori, R. & Shayegan, M. Topographic mapping of the quantum Hall liquid using a few-electron bubble. *Science* **289**, 90-94 (2000).
16 Steele, G. A., Ashoori, R., Pfeiffer, L. & West, K. Imaging transport resonances in the quantum Hall effect. *Physical review letters* **95**, 136804 (2005).
17 Zondiner, U. *et al.* Cascade of phase transitions and Dirac revivals in magic-angle graphene. *Nature* **582**, 203-208 (2020).
18 Pierce, A. T. *et al.* Unconventional sequence of correlated Chern insulators in magic-angle twisted bilayer graphene. *arXiv preprint arXiv:2101.04123* (2021).
19 Xie, Y. *et al.* Fractional Chern insulators in magic-angle twisted bilayer graphene. *arXiv preprint arXiv:2107.10854* (2021).
20 Naik, M. H. & Jain, M. Ultraflatbands and shear solitons in moiré patterns of twisted bilayer transition metal dichalcogenides. *Physical review letters* **121**, 266401 (2018).
21 Teichmann, K. *et al.* Controlled charge switching on a single donor with a scanning tunneling microscope. *Physical review letters* **101**, 076103 (2008).
22 Pradhan, N. A., Liu, N., Silien, C. & Ho, W. Atomic scale conductance induced by single impurity charging. *Physical review letters* **94**, 076801 (2005).
23 Brar, V. W. *et al.* Gate-controlled ionization and screening of cobalt adatoms on a graphene surface. *Nature Physics* **7**, 43-47 (2011).
24 Wong, D. *et al.* Characterization and manipulation of individual defects in insulating hexagonal boron nitride using scanning tunnelling microscopy. *Nature nanotechnology* **10**, 949-953 (2015).
25 Li, H. *et al.* Imaging local discharge cascades for correlated electrons in WS2/WSe2 moir\'e superlattices. *arXiv preprint arXiv:2102.09986* (2021).
26 Stomp, R. *et al.* Detection of single-electron charging in an individual InAs quantum dot by noncontact atomic-force microscopy. *Physical review letters* **94**, 056802 (2005).
27 Wang, L. *et al.* One-dimensional electrical contact to a two-dimensional material. *Science* **342**, 614-617 (2013).
28 Li, H. *et al.* Electrode-Free Anodic Oxidation Nanolithography of Low-Dimensional Materials. *Nano letters* **18**, 8011-8015 (2018).